# Plasmonic Enhancement of Irregular Shape Nano-Patch for Thin Film Silicon Solar Cells

**Nathan Burford[1] and Magda El-Shenawee[2]**

[1,2]Computational Electromagnetics Group
[1]Microelectronics-Photonics Program
[2]Department of Electrical Engineering
University of Arkansas, Fayetteville, AR, 72701, United States
nburford@uark.edu, magda@uark.edu

***Abstract*** – In this work plasmonic resonance of highly irregular aluminum nanostructures on a silicon photovoltaic substrate is investigated. These structures are inspired by natural surface structuring that occurs during the top-down aluminum induced crystallization of amorphous silicon. The computer simulations are obtained using the Ansys® HFSS allowing studying the enhanced fields transmitted into the silicon layer. The obtained results show significant light trapping and enhancement of the transmitted fields when these nanostructures are composed of high aluminum and low silicon concentration. These effects decrease for lower aluminum and high silicon concentrations cases nanostructures.

***Index Terms*** **–** Aluminum nanostructures, enhanced electromagnetic fields, plasmons, and solar energy.

## I. INTRODUCTION

Solar energy is one of the most promising sources of clean, renewable energy. Silicon (Si) thin-film technology holds potential to greatly reduce solar cell production costs, thus decreasing the cost-per-watt of solar energy enough to make it competitive against the non-renewable fossil fuels that dominate the market today [1-3]. However, a major issue of poor light absorption prevents thin-film technology from being competitive with traditional wafer based solar cells [4-8]. Due to the greatly reduced thickness of the absorbing layer, much of the incident light in a Si thin-film photovoltaic will pass through or be reflected from the interface back out before it is absorbed, thus greatly decreasing the efficiency of thin-films compared to thicker wafer based solar cells [9]. As such, novel methods for trapping light within thin-film photovoltaic are needed to make this technology advantageous over existing traditional solar cell technologies [10-12].

Recently, nanoplasmonics offer a promising method for solving some of the issues with thin-film Si technology [13-22]. By taking advantage of the plasmonic properties of the metallic nanostructures, it is possible to improve light trapping and hence photon absorption in Si thin-films. When exposed to an external electromagnetic wave (e.g., light), sub-wavelength scale metallic nanoparticles will undergo strong electrons oscillations if the frequency of the electromagnetic wave matches the plasmon frequency of the nanoparticle. First, this can lead to strong localization and enhancement of the near electric fields at the surface of the photovoltaic (PV) absorbing layer [23-25]. Second, this can cause scattering of transmitted electromagnetic waves into lateral modes, which effectively increases the path length of the transmitted wave traveling in the Si thin-film layer [10-12]. These mechanisms can improve the absorption of the light, thus increasing PV device efficiency.

Extensive work by various groups has been put forth to investigate the various parameters that influence the frequency and strength of particles plasmon resonance [26-33]. Size, shape, material properties, local dielectric environment, and local interactions with nearby particles have all illustrated strong influence on the plasmon resonance of metallic nanoparticles [13-22], and

*Submitted On: Oct. 30, 2012*
*Accepted On: Mar. 17, 2013*

[26-33]. Some examples; Cao *et al.* investigated the plasmon resonance of cylindrical, triangular, and square shaped silver nanoparticles through numerical simulation of single nanoparticles and dark-field optical microscopy of fabricated nanoparticle arrays. Their work demonstrated strong shifts in the resonant wavelength between various nanoparticle shapes and inter-particle spacing [26]. Sundar studied the effects of focused beam interactions of single metallic nanoparticles [27]. Langhammer *et al.* investigated the nanodisk geometry made of aluminum (Al) showing a strong shift in plasmon resonance from infrared to ultraviolet using varying disk aspect ratios [28]. El-Shenawee *et al.* studied, through the use of method of moments, the plasmonic interactions of single pairs of closely spaced gold nanotoroidsin [29] and finite gold nanotoroid arrays, both uniform and non-uniform in [30]. Additionally, Large *et al.* illustrated the strong shift in plasmon resonance by alteration of minor details in the nanoparticle geometry, such as rounding of nanoparticle edges that are ideally sharp 90 degree corners [31].

In addition to plasmonic resonance behavior, previous works have investigated the absorption enhancing effects for plasmonic nanoparticles located on PV devices for a wide range of cases [3, 18, 19, 34-37]. Early experimental work by Derkacs *et al.* illustrated this potential application by investigating gold spherical nanoparticles deposited on a Si thin-film, observing 8.3 % enhancement in conversion efficiency [3]. The spectral behavior of the photocurrent enhancement of gold nanospheres deposited on a Si thin-film solar cell was investigated experimentally by Lim *et al.*, with numerical simulations being performed to verify and explain the mechanisms for this enhancement [18]. Nakayama *et al.* experimentally studied this photocurrent enhancement by gold nanospheres, but for GaAs thin-films, instead of Si. In addition, it is noted that these surface localized nanoparticles reduce the surface sheet resistance of the cell, thus improving the device fill factor and providing an additional mechanism for improving the conversion efficiency [34]. Akimov*et al.* compared silver and Al nanospheres located on Sithin-films, demonstrating stronger absorption of electromagnetic energy in the Si layer by the Al nanoparticles, as well as significantly less detrimental effects by the addition of an oxide layer in the Al nanoparticles, as opposed to silver [35]. This work is continued by Akimov*et al.* to investigate the tuning of the nanoparticle geometries from the idealistic perfect sphere to elliptical nanospheroids, with the results showing optimal performance by nanoparticles of non-perfect sphere geometry [19]. Al nanospheres are also investigated and compared to gold and silver by Kocherginet *al.*, only for organic thin-film solar cells. Both experimental and theoretical results of this work show significantly higher improvement in absorption enhancement by the Al nanoparticles over gold and silver [36]. All of these works show that while plasmonic nanoparticles can indeed provide enhanced light absorption in PV devices, the performance is highly dependent on the design of the plasmonic structure. The majority of these works encompass simple, ideal geometries of plasmonic nanostructures, with less work investigating more complex irregular structures.

The current work does not deal with engineered nanostructures but it deals with irregular Al nano-patches produced during the fabrication process of the thin-film photovoltaic technology [37]. Inspiration for the structure geometry comes from an unintentional byproduct of the top-down Al induced crystallization (TAIC) of amorphous silicon (a-Si) as discussed in [37]. In traditional metal induce crystallization an a-Si thin film is deposited over a substrate, followed by the deposition of a thin metallic layer, typically on the order of tens to several hundred nanometers [38]. The bonding energy of the a-Si is much lower at the a-Si/metal interface. As such, the crystallization energy is greatly reduced. Low temperature annealing causes layer exchange between the a-Si and metallic layers and crystallizes the s-Si into polycrystalline Si [38, 39]. TAIC is a variant of metal induced crystallization in which layer exchange is minimized. Layer exchange that does occur can be controlled and result in engineered texturing [37, 39]. Movement of a-Si:H is limited by Al thickness in this case [39].

The paper is organized as follows: the computational model is presented in section II, including key analysis techniques and the full range of parameters to be investigated. In section III, the numerical results along with an interpretation of their significance are presented,

and finally concluding remarks are discussed in section IV.

## II. COMPUTATIONAL METHODOLOGY

In this work, we utilize the commercially available electromagnetic simulation software Ansys® HFSSto investigate the plasmonic enhancement properties of the highly shape irregular Al/Si composite nano-patches inspired by thin film photovoltaic (see Fig. 1 in [39]). All results are obtained using the University of Arkansas Razor High Performance Computing cluster. Each node of this computing cluster contains two hex-core Xeon X5670 processors operating at 2.93 GHz and 2x12MB cache. Four nodes of this cluster contain 96 GB of memory and these nodes specifically were the ones used in this work. Each of the single nano-patch simulations consist of approximately 680,000 mesh cells, requiring 51.2 GB of memory and 15.5 hours of computational time per frequency. Using HFSS's multiprocessing licensing this was solved using 10 processing cores, which provided a significantly reduced time of approximately 1.7 hours per frequency point.

### A. Validation

The computational study of plasmonic nanostructures offers unique challenges, as different methods can generate vastly different results if care is not taken to validate results [40]. To ensure that HFSS is being utilized correctly, specifically that an appropriate mesh cell density is used, a comparison of a single gold torus shaped nanoparticle is conducted using HFSS and a custom parallelized method of moments code (MoM) [22]. A single gold nanotoroid immersed in air is considered, since the geometry is simple yet shares a resemblance to certain features of the model of interest in this work. The toroid of interest has an outer radius of 42 nm, while the radius of the central air circle is 27 nm. Additionally, previous validation of the MoM code was performed with the Mie solution for gold nanospheres [32].

Figure 1 illustrates the results of this validation. These results are normalized scattering coefficients for each method, which allows for comparison of the resonant peak location. The observed spectral location of the peak using the

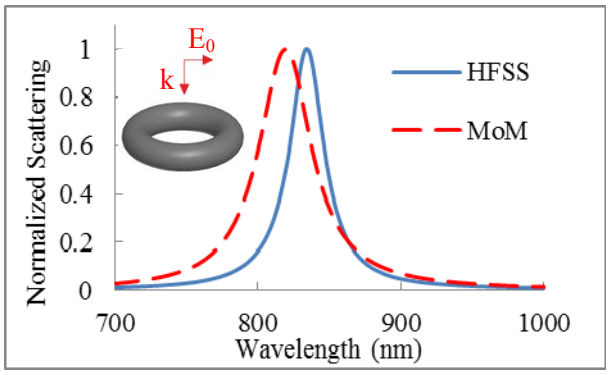


Fig. 1. Normalized scattering coefficient by a single gold toroid in air, calculated using HFSS (solid blue line) and MoM (dashed red line).

HFSS is 833 nm and using the MoM is 820 nm, indicating a 1.6 % difference in the spectral locations of the peaks. The agreement between the HFSS and MoM results confirm that the mesh density utilized here provides accurate results when applied to the other simulations presented in this work. These results are also consistent with previous studies of gold nanotoroids reported in [33].

### B. Model development

The parameters for the simulations are as follows. The computational domain extends 2000 nm in the *x* and *y* directions and 1000 nm in the *z* direction. The top portion (z = 0 to 500 nm) is modeled as air and the bottom portion (z = 0 to 500 nm) is modeled as the thin film Si photovoltaic layer. The simulation domain is excited via plane wave incident at *z* = 500, propagating in the –*z* direction and polarized along the *x*-axis. Two boundary cases are considered; (i) a single structure and (ii) an infinite array of structures. For the case of the single structure, all external surfaces of the domain are set to radiating boundary conditions. This allows scattered waves to propagate out of the simulation domain with no back reflections. Often, perfectly matched layer (PML) boundaries are used in place of radiation boundaries, as they generally provide more accurate results. However, PML boundaries require the addition of artificial layers at the external surfaces, which must be solved inside as well, increasing the computational burden of the simulation. In section III, results comparing and justifying the use of radiation boundaries as

opposed to PML boundaries are presented. The excitation for the single structure case is that of an incident plane wave propagating through the finite radiation boundary on the *x*-*y* face at $z = 500$ nm.

In the simulation of the infinite arrays, only the external surfaces at $\pm z = 500$ nm are set to radiating boundary conditions. The opposing *x*-*z* faces at $y = 0$ and 2000 nm and the opposing *y*-*z* faces at $x = 0$ and 2000 nm are both set to master/slave boundary condition pairs, so as to emulate an infinite array of nano-patches in the *x* and *y* directions by matching the fields at the slave boundary to the corresponding master boundary. This effectively mirrors the unit cell depicted in Fig. 2 (c) infinitely in the *x* and *y* directions, generating an infinite 2D square array of the nanostructures and Si substrate. The most basic method for simulating infinite arrays is to utilize perfect electric and perfect magnetic symmetry boundaries. This also effectively mirrors the computational domain infinitely in two dimensions, but requires that the excitation have electric and magnetic field components normal to the electric and magnetic symmetry planes, respectively. Master/slave boundaries allow for excitations where this requirement of normal electric and magnetic field components is not met by introducing an appropriate phase shift in the slave boundary as compared to the reference field of the corresponding master boundary. For normal angles of incidence as described in this work the phase shift between the master and slave boundaries is zero, which is effectively identical to using traditional perfect electric and perfect magnetic symmetry boundaries. However, using the master/slave boundaries allows for possible future studies of non-normal angles of incidence. In this case, the center to center separation between the nano-patch elements is 2000 nm. For the infinite arrays, these boundary conditions enforce that the plane wave excitation will be modeled as infinitely uniform in the *x* and *y* directions. Figure 2 (c), then, illustrates for the infinite 2D square array case a single unit cell of the array, with *x*-*y* size of 2000 nm by 2000 nm.

The HFSS 3D model of these highly irregular nanostructures is based on the Matlab model described by Hassan and El-Shenawee, in which 2D irregular malignancy shapes are randomly generated [41]. This model is utilized to produce a random 2D shape that resembles the SEM images

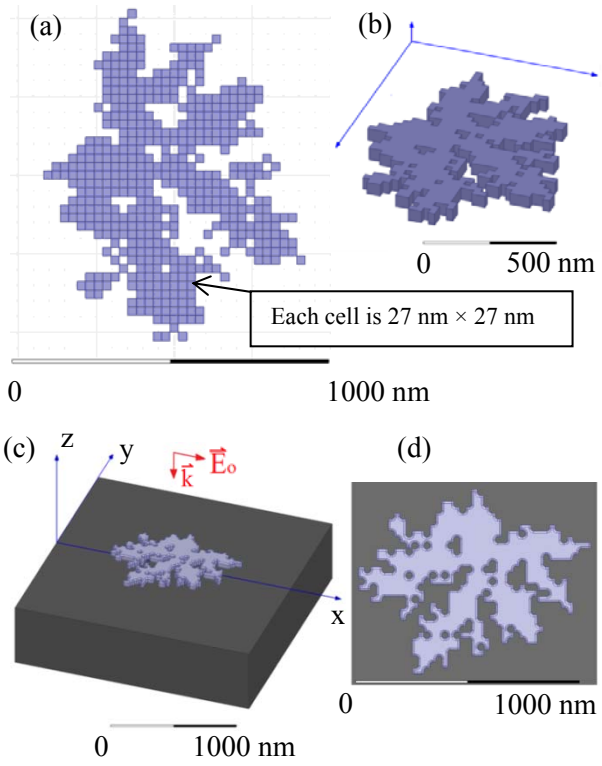


Fig. 2. HFSS model of the nano-patch to be investigated, all units in nm. (a) Top view of 2D nano-patch pattern constructed using 27 nm by 27 nm unit cells, (b) initial 3D model, produced by Boolean addition of unit cells and 50 nm extrusion along the *z*-direction, (c) final computational model, 10 nm radius rounding of all sharp edges and placement a top 500 nm thick silicon layer, (d) top view of finalized 3D model.

of the nanostructures (see Fig. 2 in [37]). The output data of the model is in the form of an array of coordinates for each of the individual square sheets that together form the entire nano-patch structure. The coordinates are then scaled to a typical nanostructure size and from here the coordinate data is used as a guide for placing 27 nm by 27 nm square sheets in the *x*-*y* plane at $z = 0$ nm in the HFSS model. These separate squares collectively form the basis of the entire irregular nano-patch structure, as shown in Fig. 2 (a). This is a time consuming process, as this model is based on approximately 535 of these individual square sheets, each of which must be manually placed in its appropriate location. Once all unit cells are in place, they are combined using the Boolean add feature and extruded 50 nm along the

z-direction, thus producing a 3D object from the 2D sheet, illustrated in Fig. 2 (b). Finally, all edges of the structure are rounded to a 10 nm radius curvature, so as to reduce unrealistic edge effects that can arise from the presence of sharp corners. This final 3D model of the nanostructure is illustrated in Fig. 2 (c), with a top view of the final structure shown in Fig. 2 (d).

As known, purely noble metallic particles exhibit plasmonic resonance. However, the surface structures observed during the TAIC process are not purely Al, but instead some mixture of Al and Si. As such, we consider not only cases of purely Al nano-patches, but also nano-patches of 30 % and 5 % Al, with the remainder being Si. For these mixture cases, the electrical properties for the nano-patch are calculated by taking a weighted average of the Al and Si properties. Both the Si and Al are frequency dependent in this band. We approximated the nanostructure to be a function of Al percentage, comprising the material (%Al); we used effective permittivity calculated using associated weights, of material percentage, of the electrical properties of pure Al and pure Si given by,

$$\varepsilon_{eff}(\%Al) = \varepsilon_{Al}\,\%Al + \varepsilon_{Si}(1 - \%Al). \quad (1)$$

Here, $\varepsilon_{Al}$ represents the permittivity of pure Al and $\varepsilon_{Si}$ is the permittivity of pure Si. The frequency dependent values for the electrical properties of Si and Al are taken from Palik [42]. Figures 3 and 4 illustrate the frequency dependent real and imaginary parts of the electrical permittivity for pure Si and pure Al, as well as the effective permittivity of the nanostructure at 30 % and 70 % Si and 5 % Al and 95 % Si, respectively.

The results are quantitatively compared by calculating the frequency dependent enhancement factor, EF(λ) for each of the cases. Inside the Si layer the only field that exists is either the fields scattered by the Si surface alone (reference case) or the fields scattered by both the Si surface and the nano-patch (enhanced case). The EF(λ) is calculated as the ratio of the average scattered field intensity absorbed in the Si layer with and without the nanostructure presented in [18],

$$\mathrm{EF}(\lambda) = \frac{\int \left|\boldsymbol{E}_{\mathrm{Si_{with}}}\right|^2 \mathrm{dV}}{\int \left|\boldsymbol{E}_{\mathrm{Si_{without}}}\right|^2 \mathrm{dV}}. \quad (2)$$

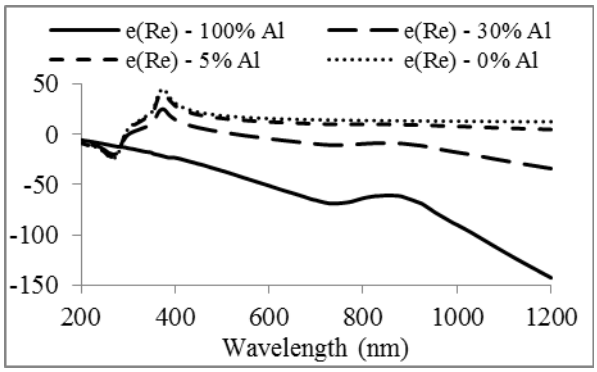


Fig. 3. Real part of the relative permittivity pure Al (solid line), pure a-Si (dotted line) and 30%, 5% Al weighted averages calculated using equation (1).

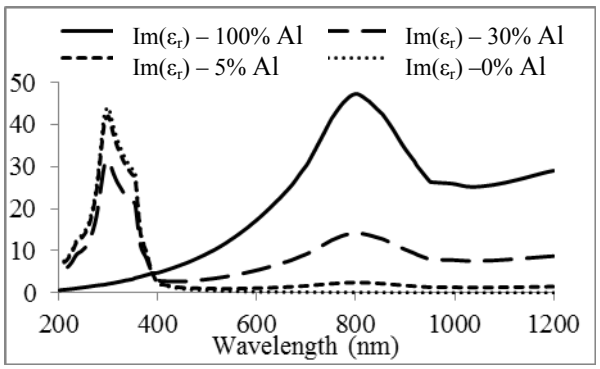


Fig. 4. Imaginary part of the relative permittivity pure Al (solid line), pure a-Si (dotted line) and 30%, 5% Al weighted averages calculated using equation (1).

In addition to the calculation of EF(λ), visual comparisons of wave interaction with the surface structure will be shown in section III.

## III. NUMERICAL RESULTS AND DISCUSSION

In this section, the enhancement factor, EF(λ),will be shown for single and infinite arrays of the nano-patch geometry defined in Figs. 2 (c) and 2 (d) where the computational domain is 2000 nm × 2000 nm × 1000 nm. Three cases of Al composite material will be considered for the nano-patch positioned on top of Si as 100 %, 30 % and 5 %.

### A. Enhancemnet factor EF(λ)

The results of Fig. 5 show the enhancement factor, EF(λ), for six cases versus the wavelength from 500 nm to 1200 nm. The plot of diamond symbols (red color) represents the 100 % Al nano-patches, the plot in of square symbols represents the 30 % Al and 70 % Si (green color), and the plot of triangular symbols represents (blue color) represent nano-patches made of 5 % Al and 95 % Si. The nano-patch structure, depicted in Fig. 2, has highly irregular shape with several air gaps in the structure that could contribute to the observed multiple resonances. Consider Fig. 2 (d), the top view of the nano-patch, the light blue coloring represents the nano-patch and the dark gray represents the Si substrate. The incident wave is propagating down into the structure with horizontal polarization across the nano-patch. It is observed that there are several different locations on the nano-patch where the electric field is applied across air gap locations. When the nano-patch is considered made of 100 % Al, this will cause capacitive coupling with the incident light at certain frequencies. Due to the variance of sizes and shapes of the air gap locations there is a variance in the capacitive resonances as well, which could explain why multiple peaks are observed in the EF(λ) plots in Fig. 5.

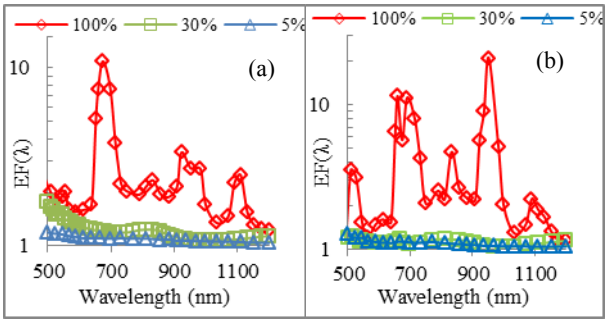


Fig. 5. Enhancement factor EF(λ) for nano-patch surface structures composed of 100 %, 30 %, and 5% aluminum for (a) single nano-patch and (b) infinite array of nano-patches.

The results show a maximum peak at a wavelength of 674 nm for the single nano-patch as shown in Fig. 5 (a) and at a wavelength of 952 nm for the array as shown in Fig. 5 (b). As anticipated, when the material of the nano-patches are assumed made of 30 % and 70 % Si or 5 % Al and 95 % Si, the resonance peak is much smaller and occurs at a wavelength 810 nm for both the single and infinite array cases. As reported in El-Shenawee *et al.* in [30], the resonance of an array of nanotoroids of the far fields occurs at the same wavelength of a single nanotoroid when the separation distance between elements is in the order of a wavelength. Therefore, the results reported in [30] show accumulative behavior in the extinction coefficient in the case of such array. However, the results of Fig. 5 show distinct differences between the resonances and peaks of the single nano-patch and the infinite array cases. Note that the results of Fig. 5 are for fields at 500 nm away from the interface, which is considered near fields. The wave propagation inside the Si layer exhibit a strong likelihood inter-particle coupling that can also explain the observed differences in the plasmons in Figs. 5 (a) and 5 (b), as will be shown in wave propagation graphs of Figs. (8) to (15).

Note that the enhancement factor (EF) of equation (2) is the wave absorption in Si with the presence of the nano-patch compared with that without it. The results of Fig. 5 show slight increase in the EF for both of the 5 % Al cases, with slight improvement in the 30 % Al cases. For these cases, the majority of the electrical properties of the structures come from Si, which has low electrical permittivity in the frequency range considered. As such, plasmonic effects that arise from the presence of the Al are reduced. The enhancement that does take place increases slightly as the wavelength decreases. At shorter wavelengths the many smaller features and holes in the structure of Fig. 2 contribute to slight scattering of the transmitted fields, which yield a small increase of the transmitted energy into the Si layer. At the longer wavelengths these small features become negligible due to the low Al composition. The features produce little effect on the transmitted fields and as such there is little difference between the case with the nano-patch and the reference case making the EF close to 1 as shown in Fig. 5.

### B. Comparison of boundary conditions

A particular concern in HFSS is the application of proper boundary conditions, in particular the external absorbing boundaries. HFSS provides several options for absorbing boundaries, of particular interest here are the

radiation boundary condition and the perfectly matched layer (PML) boundaries. In Fig. 6, a comparison of the radiation boundaries and the PML boundaries is shown for the EF(λ). In this case a single 100 % Al nano-patch is investigated; once using the radiation boundaries as external boundaries and again using the PML boundaries. The results show good agreement between the two cases, with some minor deviation. The radiation boundaries are recommended for situations where scattering bodies are more than λ/4 away from the boundary, which is the case for this work. Using the radiation boundary requires approximately 0.68 million mesh cells and 51.2 GB of memory, while using the PML boundaries requires approximately 1.12 million mesh cells and 131 GB of memory. This is due to the addition of the artificial absorbing layer around the simulation domain, which must be accurately meshed as well. Although this absorbing layer does theoretically represent a more accurate solution, the radiation boundaries give nearly as good results at less than half the computational resources. As such, the radiation boundaries are adopted for this work.

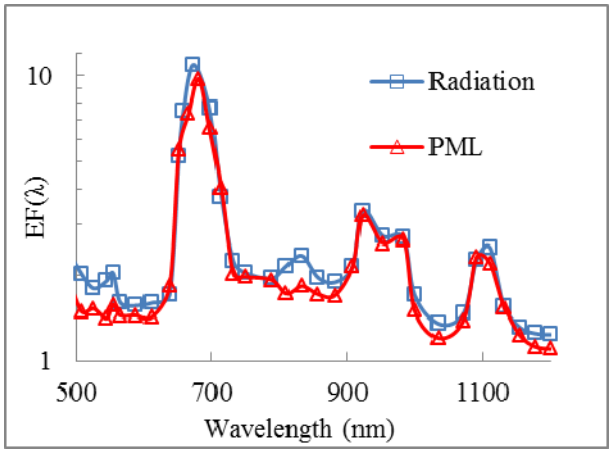


Fig. 6. Enhancement factor for a single 100 % aluminum nano-patch using radiation boundaries and PML boundaries.

### C. Two irregular nano-patches

The infinite uniform array approximation is used here to manage the computational requirement, but it would be more practical to investigate the coupling between non-identical nanostructures. Here, two different irregular structures are generated using the same method described in section II. Both structures are approximately 450 nm and 600 nm across, respectively, 50 nm thick in the *z* direction and 900 nm center to center spacing with the incident excitation polarization oriented across the gap (see Fig. 7 (a)). The electrical properties used for the nano-patch structures are 100 % Al, with electrical properties depicted by the solid black line in Figs. 3 and 4. The Si layer is 1800 nm by 2600 nm by 500 nm, the air region above the Si is 500 nm thick in the *z* direction. For consistency in this work, the external boundaries are set to absorbing radiation boundaries. The configuration is illustrated in Fig. 7 (a). The high computational cost of this model restricts the overall size and number of different nano-patches that can be modeled, however, by implementing more efficient solvers it may be possible to increase the complexity of these models [43].

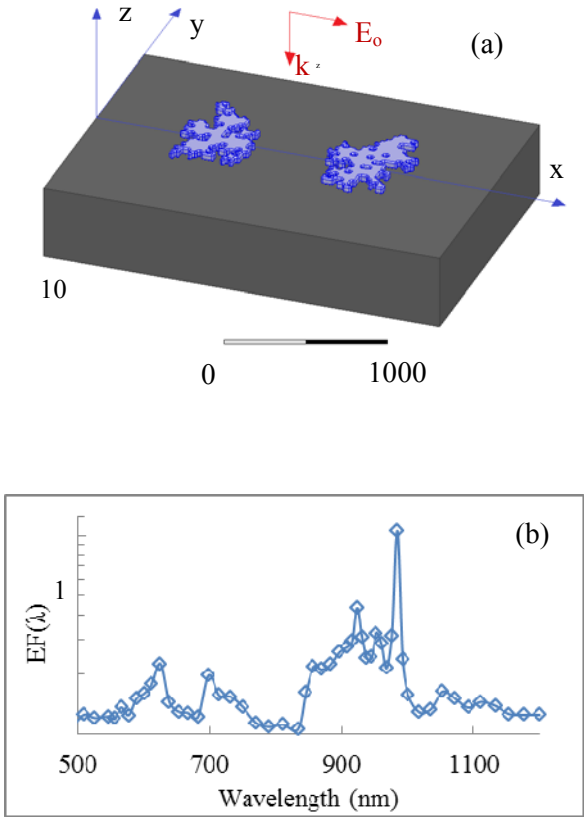


Fig. 7. (a) Computational configuration of a finite dual 100 % Al nano-patch simulation and (b) EF(λ) results of Fig. 7 (a).

In this case, the enhancement factor is calculated using equation (2) and the results are illustrated in Fig. 7 (b). Between λ = 770 nm and λ = 833 nm EF(λ) falls below 1, indicating to deterioration in efficiency, reaching its lowest value of 0.84 at λ = 833 nm. Aside from this range, the EF(λ) is above 1, indicating enhancement of the electromagnetic fields in the Si layer for most of the considered spectrum. On the other hand, between wavelengths of 845 nm and 992 nm a varying level of enhancement is observed. Upon comparison with Fig. 6, the EF(λ) levels of the single 100 % Al nano-patch occurs between 909 nm and 980 nm.

### D. Wave propagation in silicon due to a single nano-patch

Figures 8 and 9 illustrate 2D plots of the magnitude of the real part of the electric fields for single nano-patch made of 100 % and 30 % Al, respectively. Due to space limitations, all 2D electric field plots for the 5 % Al cases are excluded, as in these cases the structure minimally affects the transmitted electromagnetic wave. The plots are shown in the *x*-*z* plane at *y* = 0 nm. The results shown in Figs. 8 and 9 are obtained at wavelengths of 682 nm and 810 nm, respectively. A sweep over the phase of the incident plane wave is conducted in steps of 60 degrees in the range from 0 to 120 degrees. This sweep shows the wave propagation in the computational domain. Due to the difference in the values of the electric fields in air and in Si, two different scales are shown in the figures, one for air and one for Si. The fields inside the nano-patch itself is not shown here. Figure 8 shows the 100 % single Al nano-patch case at a wavelength of 682 nm and Fig. 9 shows the 30 % single Al nano-patch at a wavelength of 810 nm. The observed wavelengths are at peaks in the enhancement factor for each of the cases.

Figure 8 illustrates the fields at the plasmonic resonance of the single 100 % Al nano-patch at λ = 682 nm, which is associated with the largest peak in the enhancement factor (EF) in Fig. 5 (a) (red color curve). The graph of Fig. 8 provides insight to the propagation behavior of the electromagnetic waves transmitted into the Si layer. Notice the oblique angle of the wave propagation into the Si when the nano-patch is present (see the arrow in Fig. 8 (a)). This observation can indicate the increase of light path in the Si and hence more absorption of the photon energy and increase in photocurrent generation.

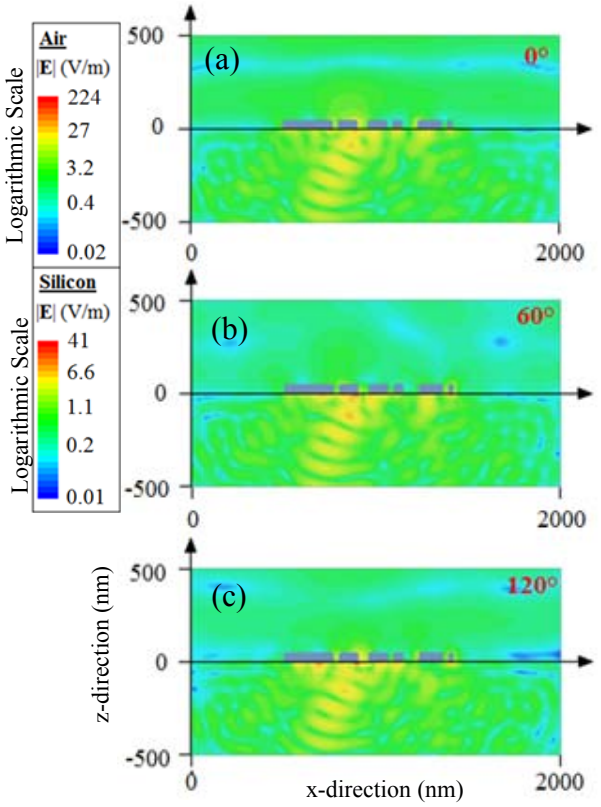


Fig. 8. Real part of the electric field on the *x*-*z* plane at y = 0 nm. Sweep over the phase at λ = 682 nm. Single nano-patch of 100 % aluminum composition.

A significantly reduced scattering in the 30 % Al nano-patch is shown in Fig. 9 (3.1V/m) compared with the 100 % Al shown in Fig. 8 (41V/m). This is supported by the EF(λ) plot of Fig. 5, where no distinct resonant peaks observed for the 30 % Al.

The phase sweep for the 30 % Al single nano-patch cases is shown in Fig. 9. For this 30 % Al case, lateral propagation of the transmitted wave is still observed, although not nearly as prominent as the 100% Al case. Similarly, the 5 % Al case (not shown for space limits) demonstrates even more reduction in the scattering in the *x*-*z* directions (i.e., lateral scattering). Additionally, the minimal scattering and enhancement for both cases that does take place does not extend far away from the structure, returning to plane wave propagation further away from the nanostructure; unlike in the

single 100 % Al nano-patch case. As such, it is expected that scattering for the 30 % and 5 % Al cases will not have drastic differences between the single and infinite array cases.

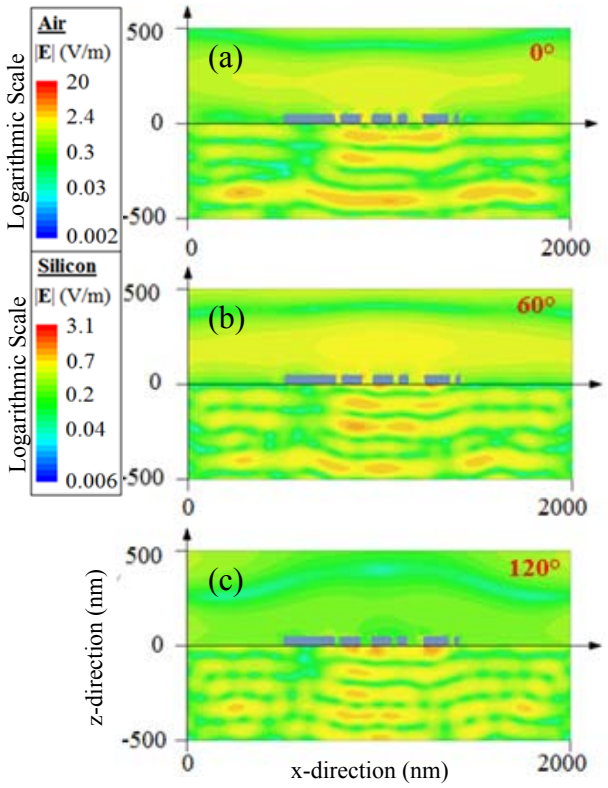


Fig. 9. Real part of the electric field on the *x*-*z* plane at y = 0 nm. Sweep over the phase at λ = 810 nm. Single nano-patch of 30 % aluminum composition.

### E. Wave propagation in silicon due to infinitearray of nano-patches

The graphs of wave propagation (phase sweep) in Si of the single nano-patch are repeated here for the infinite array. The results of Figs.10 and 11 illustrate similar 2D plots of the magnitude of the real part of the electric fields, for the same three composite material cases. All graphs are confined under one element of the array for comparison reasons. Figure 10 shows the 100 % Al nano-patch case at a wavelength of 697 nm and Fig. 11 shows the 30 % Al nano-patch at a wavelength of 810 nm. These wavelengths are the observed peaks in the enhancement factor for each of the cases shown in Fig. 5 (b).

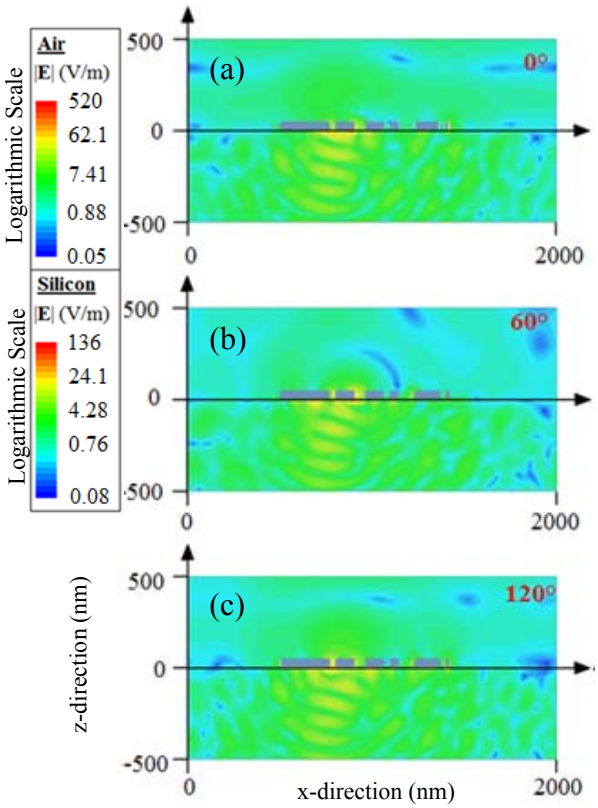


Fig. 10. Real part of the electric field on the *x*-*z* plane at y = 0 nm. Sweep over the phase at λ = 697 nm. Infinite nano-patch array of 100 % aluminum composition.

Just as with the single nano-patch cases, in the infinite array cases strongest lateral propagation is observed for the 100 % with reduced scattering for the 30 % case and 5 % case (not shown). Consider Fig. 10, which illustrates the 2D fields for the 100 % Al infinite array case at the peak in the EF(λ) plot. This peak is shifted by approximately 15 nm as compared to the single nano-patch case. In addition, note that the pattern of the transmitted fields is somewhat different.The scattering of the transmitted waves in the single 100 % Al nano-patch case appears to be slightly more in the lateral directions as compared to the infinite array case of Fig. 10. Additionally, the peak magnitudes of the electric fields are significantly different; 41 V/m for the single 100 % Al nano-patch case versus 136 V/m for the infinite array case, as expected.

In the 30% Al nano-patch array illustrated in Fig. 11, there again is greatly reduces scattering for the 30 % case as compared to the 100 % case

and even more reduction in the 5 % case. As compared to the single nano-patch counter part of the 30 % Al nano-patch array from Fig. 9, the infinite array field graphs of the 30 % Al nano-patches have some distinct similarities as well as some differences. In both cases the maximum field values are the similar, 4.0 (V/m) and 3.1 (V/m) for the 30 % Al infinite array and single nano-patch cases, respectively and 0.87 (V/m) and 0.83 (V/m) for the 5 % Al infinite array and single nano-patch cases, respectively. Differences do exist in the field patterns for the two cases. In the 30 % Al single nano-patch case (Fig. 9) note that the fields decay at the $x$ = 0 nm and $x$ = 2000 nm faces, as opposed to the infinite array cases (Fig. 11) where the fields continue uniformly at these faces. The same is observed in the 5 % Al nano-patch cases.

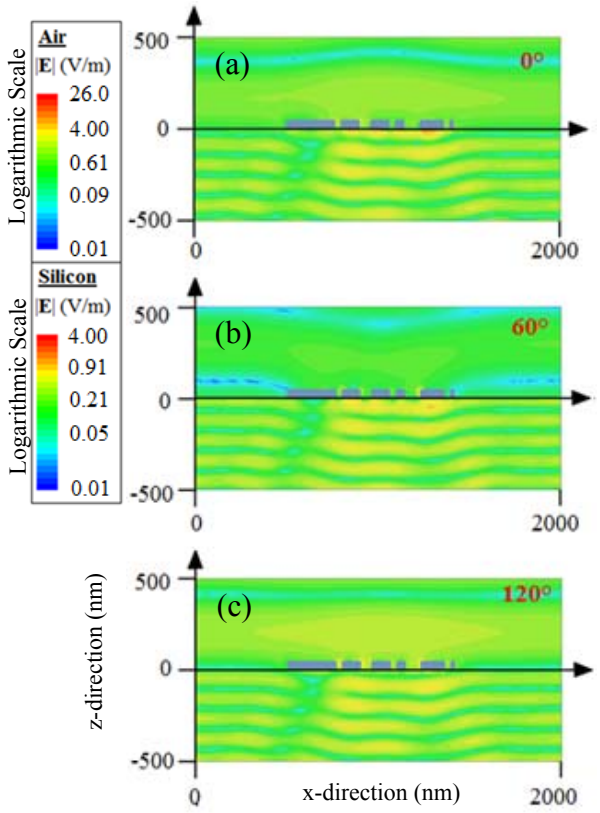


Fig. 11. Real part of the electric field on the $x$-$z$ plane at y = 0 nm. Sweep over the phase at λ = 810 nm. Infinite nano-patch array of 30 % aluminum composition.

### F. Field in silicon due to single nano-patch versus wavelength

In this sub-section, we show the magnitude of the fields versus the wavelength as shown in Figs. 12 and 13 for the single nano-patch cases of 100 % and 30 % Al, respectively. For each of the two cases, three different incident wavelengths are observed. The electric field graphs for these various material composites of the nano-patches provide insights into the various mechanisms of field enhancement in the Si layer.

In Fig. 12, the 100 % single Al nano-patch, the 2D electric field plots are observed for incident wavelength values of 682 nm, 750 nm, and 952 nm. The plots at 682 nm and 952 nm associated with select enhancement peaks in Fig. 5 (a), while the 750 nm plot is a non-resonant value for the sake of comparison. Visually, these field plots match well with what would be expected after considering the enhancement factor in Fig. 5 (a). The strong EF(λ) peak observed at 682 nm in Fig. 5 (a) is visual confirmed in Fig. 12 (a). Here, we observe not only strong enhancements of the near fields at the nano-patch/silicon interface but also significant enhancement of the propagating waves transmitted into the Si layer. The second observed peak is shown in Fig. 12 (c) for 952 nm. This shows significant enhancement of the transmitted propagating waves, though reduced in magnitude from that, which occurs at λ = 682 nm. At λ = 1111 nm there is another slight peak in EF(λ) observed in Fig. 5 (a). In the field plot of this wavelength (not shown) the enhancement seems to be localized more closely to the structures than in the other three observed peaks, which show strong enhancement of the waves transmitted deeper in the Si layer.

Figure 13 shows similar 2D field graphs for the 30 % Al single nano-patch case. In the 100 % Al single nano-patch case the highest values of the electric field is approximately 41 V/m while for the 30 % Al single nano-patch case it is around 9 V/m. From Fig. 5 (a), the main peak in EF(λ) for the 30 % Al case occurs at λ = 833 nm. This is supported by Fig. 13 (b), where we see slightly higher magnitudes in the fields transmitted into the Si layer as opposed to the other observed wavelengths. Compared to the 100 % Al case, there is not nearly as dramatic differences between the observed wavelengths in the 30 % Al single nano-patch case. This can be attributed to the

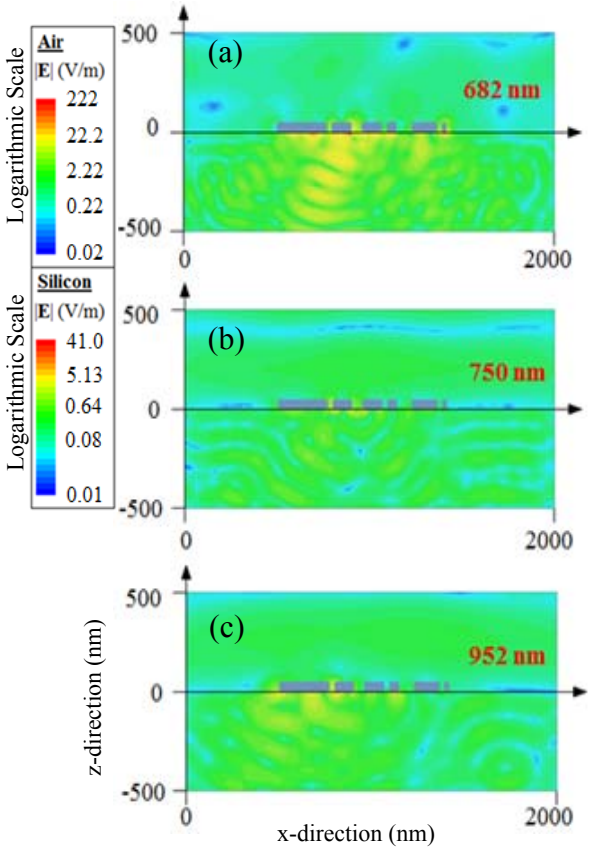


Fig. 12. Real part of the electric field on the *x*-*z* plane at y = 0 nm. Sweep over the wavelength at constant phase. Single nano-patch of 100 % aluminum composition.

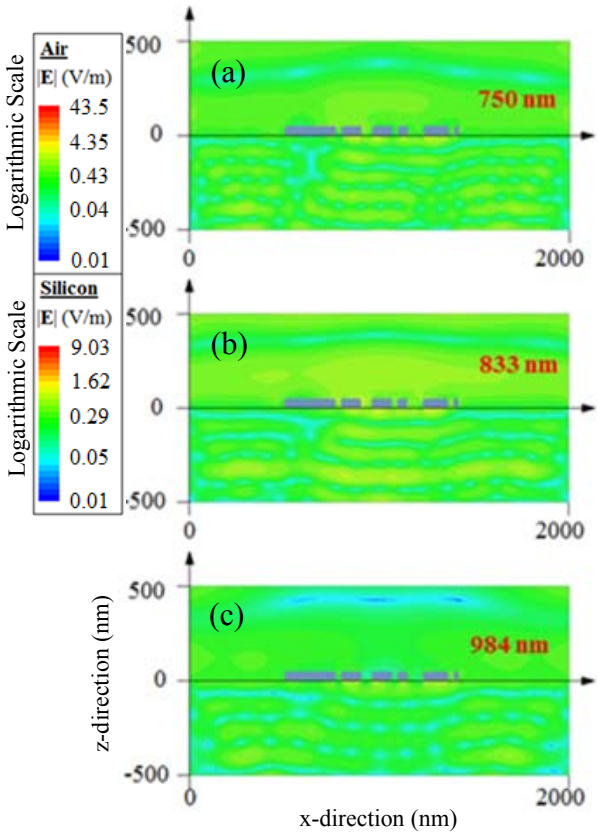


Fig. 13. Real part of the electric field on the *x*-*z* plane at y = 0 nm. Sweep over the wavelength at constant phase. Single nano-patch of 30 % aluminum composition.

greatly reduced magnitude of resonance of the structure as shown in Fig. 5 (a). From the 2D electric field graphs for various wavelengths in the 5 % Al single nano-patch case (not shown), we see a significant decrease in the maximum electric field value in the Si layer for this case, 0.8 V/m, as compared to 9 V/m for the 30 % Al case, 9 V/m. This trend indicates that for Al-Si mixed nanostructures, plasmonic enhancement is strongly dependent on the concentration of Al within the nano-structure.

### G. Field in silicon due to infinite array versus wavelength

The magnitude of the electric field is plotted in Figs. 14 and 15 associated with infinite nano-patch array of the 100 % and 30 % Al nano-patch compositions. The fields are obtained at various wavelengths of the incident plane wave. A key difference between the field graphs and the single nano-patch graphs in Figs. 12 and 13 is the possibility of electromagnetic coupling between adjacent nanostructures in the infinite array configuration as discussed earlier. Interactions such as these can have significant effects on the spectral location and magnitude of plasmonic resonances. Consider the EF(λ) plots in Fig. 5 for the two 100 % Al nano-patch for single and array cases. The major peak in the single element of 100 % Al nano-patch occurs at λ = 674, with other peaks at λ = 833, 923, and 1111 nm (see Fig. 5 (a)). By comparison, the infinite array results from Fig. 5 (b) illustrate peaks at locations λ = 697, 833, 952, and 1090 nm, which are close, but not the same, to those of the single nano-patch peaks of Fig. 5 (a). The peaks occurring at λ = 833 nm and λ = 952 nm show considerably increased magnitude as compared to the comparative peaks in the single nano-patch case, as anticipated. The peak in the single nano-patch case occurring at λ =

674 nm is slightly shifted in the infinite array case to λ = 697 nm. Additional peaks are observed in the infinite array case at λ = 659 and 508 nm. The shift in the resonance peaks between the single and array cases are consistent with *El-Shenawee et al* [29].

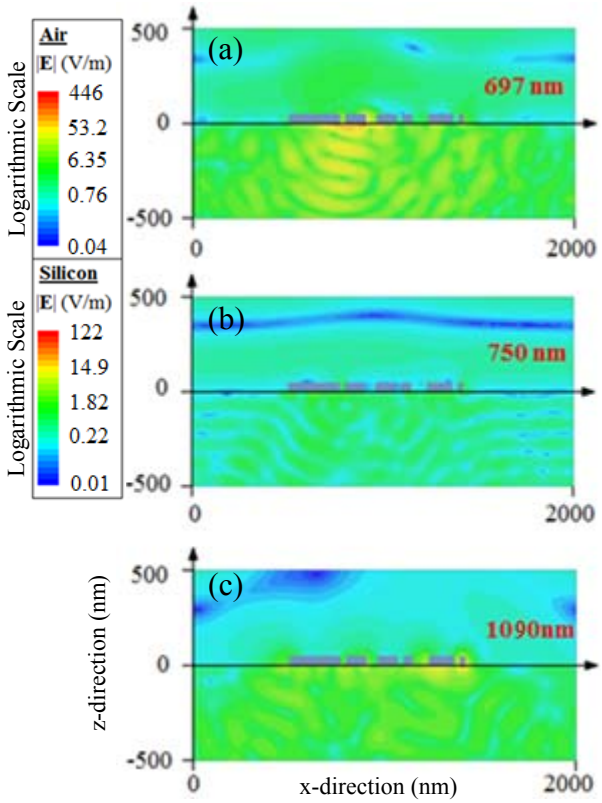


Fig. 14. Real part of the electric field on the *x*-*z* plane at y = 0 nm. Sweep over the wavelength at constant phase. Infinite nano-patch array of 100 % aluminum composition.

Figure 14 (b) illustrates an incident wavelength of 750 nm. This wavelength represents a non-resonant point in the EF(λ) of Fig. 5. Note at these wavelengths that although the structure does cause some scattering of the incident plane wave, this scattering seems to be located close to the nanostructure surface and does not extend to the periodic boundaries at the *x* = 0 and 2000 nm and *y* = 0 and 2000 nm extremities. Figures 14 (a) and 14 (c) are associated with the incident wavelengths of 697 and 1000 nm, respectively, where peaks in the EF(λ) in Fig. 5 (b) plot occur. At these wavelengths, the nano-patch structure exhibits strong scattering of the incident plane wave. This scattering clearly extends to the periodic boundaries, thus indicating that coupling between adjacent particles is possible in the nano-patch array case. Consider this infinite array case compared to the single nano-patch case depicted in Fig. 12. In both cases we see very similar patterns in the scattering of the transmitted field in the Si layer. The major difference between the two lies in the peak values of the electric fields in both cases. In the single nano-patch case, the peak electric field in the Si layer is ~41 V/m, while the peak value in the infinite array case is approximately 122.5 V/m. The observed wavelengths are not exactly the same, 682 nm for the single nano-patch and 697 for the array.

Similar plots are shown in Fig. 15 for the 30 % Al nano-patches infinite array. Upon comparing the maximum transmitted fields in Si between the three infinite nano-patch array cases, the maximum field value occurs in Fig. 14 as 122 V/m, in Fig. 15 as 4 V/m and in the 5 % Al nano-patch array case as 0.888 V/m (not shown). Note

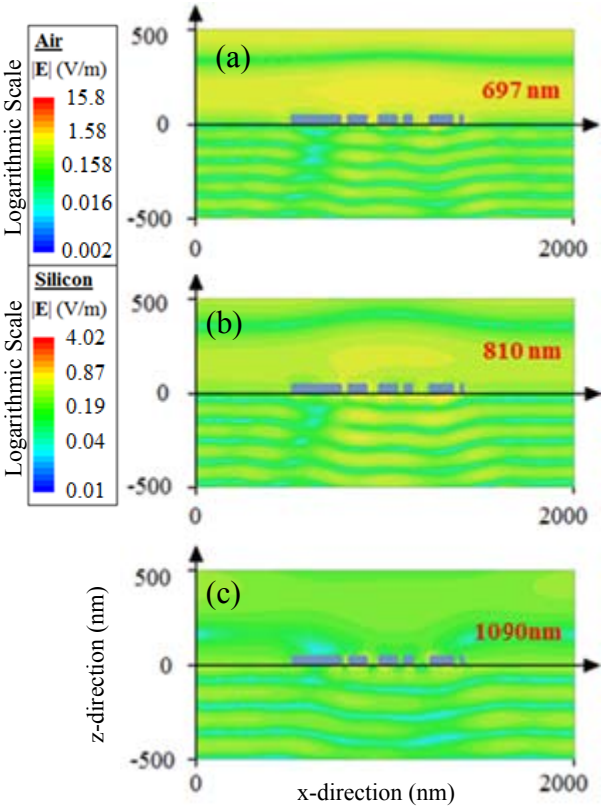


Fig. 15. Real part of the electric field on the *x*-*z* plane at y = 0 nm. Sweep over the wavelength at constant phase. Infinite nano-patch array of 30 % aluminum composition.

that in Fig. 15 the scattering of the transmitted wave caused by the nanostructure does not extend to the periodic boundaries located at the $x = 0$ and 2000 nm and $y = 0$ and 2000 nm extremities for all observed wavelengths, with a similar observation made for the 5 % Al nano-patch array. As such, the coupling between adjacent structures is not present in the 30 % Al case compared with the 100 % Al case. This explains the similarities observed between Figs. 13 and 15 and also the similar plots of EF(λ) for both the single and infinite array of 30 % Al nano-patch cases.

Figure 14 also illustrates the mechanism by which this irregular geometry has multiple resonance peaks. Consider Fig. 14 (a), which shows excitation at λ = 697 nm. Here, the strongest field enhancements are located just left of the center point of the nano-patch at approximately $x$ = 900 nm, $y$ = 0 nm. This indicates that the local nano-patch geometry at this location resonates strongly at 697 nm, much stronger than other locations on the nano-patch. Now consider Fig. 14 (c) associated with incident wavelength of 1000 nm, which is another strong resonant peak in the 100 % Al infinite array case. Here, the strongest resonance occurs are the far right of the nanostructure at approximately $x$ = 1400, $y$ = 0 nm. This change in the physical location of the plasmon resonance indicates that in highly irregular nanostructure geometries, where holes can represent cavity-like structure, can support localized enhanced fields at various locations on the structure.

## IV. CONCLUSION

In this work, we have investigated the enhancement of electromagnetic energy transmission into an Si thin-film layer due to highly irregular surface nanostrucutres. These structures, inspired by naturally occurring structuring formed during the thin film fabrication technology process, show localized field enhancement in the Si layer when the nanostructure composite includes more Al than Si. The enhanced field magnitude being the highest observed for nano-patches of 100 % Al composition and is reduced greatly as the Al/Si ratio of the nano-patch is decreased. Since the experimentally observed structures forming from the TAIC process are predicted to have a low Al concentration (< 5 %) the results of this work indicate that the presence of these structures would cause neither significant enhancement nor degradation of energy absorption in a Si thin film [39]. However, pure Al irregular nanostructures hold promising potential for providing absorption enhancement in thin-film Si solar cells, particularly in the development of multi and wide-band resonating nanostructures.

## ACKNOWLEDGEMENT

This work is supported mainly through the NSF/ECCS award no. 1006927 and in part through NSF GK12 award no. 0538645, NSF Cyber infrastructure awards EP-0918970 and MRI no. 072265.

### REFERENCES

[1] G. Crabtree and N. Lewis, "Solar energy conversion," *Physics Today*, pp. 37-42, Mar., 2007.

[2] D. Kotter, S. Novack, W. Slafer, and P. Pinhero, "Solar nantenna electromagnetic collectors," *Proc. 2nd Int. Conf. Energy and Sustainability*, pp. 1-7, Jacksonville, FL, 2008.

[3] D. Derkacs, S. Lim, P. Matheu, W. Mar, and E. Yu, "Improved performance of amorphous silicon solar cells via scattering from surface plasmon polaritons in nearby metallic nanoparticles," *Appl. Phys. Lett.*, vol. 89, no. 093103, pp. 1-3, Aug. 2006.

[4] W. Warrick, R. Kappera, and M. Tayahi, "Enhanced optical absorption in thin film solar cells by surface plasmons," *in International Conference on Photonics*, Langkawi, pp. 1-5, 2010.

[5] B. Rand, P. Peumans, and S. Forrest, "Long-rang absorption enhancement in organic tandem thin-film solar cells containing silver nanoclusters," *J. Appl. Phys.*, vol. 96, no. 12, pp. 7519-7526, Dec. 2004.

[6] J. Zhu, M. Xue, H. Shen, Z. Wu, S. Kim, J. Ho, A. Hassani-Afshar, B. Zeng, and K. Wang, "Plasmonic effects for light concentration in organic photovoltaic thin films induced by hexagonal periodic metallic nanospheres," *Appl. Phys. Lett.*, vol. 98, no. 151110, pp. 1-3, Apr. 2011.

[7] A. Ostfeld and D. Pacifici, "Plasmonic concentrators for enhanced light absorption in ultrathin film organic photovoltaics," *Appl. Phys. Lett.*, vol. 98, no. 113112, pp. 1-3, Mar. 2011.

[8] M. Dühring, N. Mortensen, and O. Sigmund, "Plasmonic versus dielectric enhancement in thin-film solar cells," *Appl. Phys. Lett.*, vol. 100, no. 211914, pp. 1-4, May 2012.

[9] G. Beaucarne, "Silicon thin-film solar cells," *Advances in Opto. Electronics*, vol. 2007, no. 36970, pp. 1-12, Aug. 2007.

[10] V. Ferry, M. Verschuuren, H. Li, E. Verhagen, R. Walters, R. Schropp, H. Atwater, and A. Polman, "Light trapping in ultrathin plasmonic solar cells," *Optics Express*, vol. 18, no. S2, pp. A237-A245, June 2010.

[11] S. Mokkapati, F. Beck, A. Polman, and K. Catchpole, "Designing periodic arrays of metal nanoparticles for light-trapping applications in solar cells," *Appl. Phys. Lett.*, vol. 95, no. 053115, pp. 1-3, Aug. 2009.

[12] S. Mokkapati, F. Beck, R. Waele, A. Polman, and K. Catchpole, "Resonant nano-antennas for light trapping in plasmonic solar cells," *J. Phys. D: Appl. Phys.*, vol. 44, no. 185101, pp. 1-9, Apr. 2011.

[13] H. Atwater and A. Polman, "Plasmonics for improved photovoltaic devices," *Nature*, vol. 9, pp. 205-213, Mar. 2010.

[14] S. Pallai and M. Green, "Plasmonics for photovoltaic applications," *Solar Energy Materials and Solar Cells,* vol. 94, pp. 1481-1486, Mar. 2010.

[15] F. Tsai, J. Wang, J. Huang, Y. Kiang, and C. Yang, "Absorption enhancement of an amorphous Si solar cell through surface plasmon-induced scattering with metal nanoparticles," *Optics Express*, vol. 18, no. S2, pp. A207-A220, 2010.

[16] F. Beck, E. Verhagen, S. Mokkapati, A. Polman, and K. Catchpole, "Resonant SPP modes supported by discrete metal nanoparticles on high-index substrates," *Optics Express*, vol. 19, no. S2, pp. A146-A156, Feb. 2011.

[17] H. Fischer and O. Martin, "Engineering the optical response of plasmonic nanoantennas," *Optics Express*, vol. 16, no. 12, pp. 9144-9154, June 2008.

[18] S. Lim, W. Mar, P. Matheu, D. Derkacs, and E. Yu, "Photocurrent spectroscopy of optical absorption enhancement in silicon photodiodes via scattering from surface plasmon polaritons in gold nanoparticles," *J. Appl. Phys.*, vol. 101, no. 104309, pp. 1-7, May 2007.

[19] Y. Akimov and W. Koh, "Design of plasmonic nanoparticles for efficient subwavelength light trapping in thin-film solar cells," *Plasmonics*, vol. 6, pp. 155-161, Oct. 2010.

[20] M. Yang, Z. Fu, F. Lin, and X. Zhu, "Incident angle dependence of absorption enhancement in plasmonic solar cells," *Optics Express*, vol. 19, no. S4, pp. A763-A771, July 2011.

[21] J. Khurgin and G. Sun, "Impact of disorder on surface plasmons in two-dimensional arrays of metal nanoparticles," *Appl. Phys. Lett.*, vol. 94, no. 221111, pp. 1-3, June 2009.

[22] N. Burford and M. El-Shenawee, "Parallel MoM computation of localized field in silicon due to finite array of nanotoroids," *Proc. 29th Annual Review of Progress in Applied Computational Electromagnetics*, March 24-28, 2013.

[23] J. Wang, F. Tsai, J. Huang, C. Chen, N. Li, Y. Kiang, and C. Yang, "Enhancing InGaN-based solar cell efficiency through localized surface plasmon interaction by embedding Ag nanoparticles in the absorbing layer," *Optics Express*, vol. 18, no. 3, pp. 2682-2694, Feb. 2010.

[24] N. Lal, B. Soares, J. Sinha, F. Huang, S. Mahajan, P. Bartlett, N. Greenham, and J. Baumberg, "Enhancing solar cells with localized plasmons in nanovoids," *Optics Express*, vol. 19, no. 12, pp. 11256-11263, June 2011.

[25] Z. Ouyang, S. Pillai, F. Beck, O. Kunz, S. Varlamov, K. Catchpole, P. Campbell, and M. Green, "Effective light trapping in polycrystalline silicon thin-film solar cells by means of rear localized surface plasmons," *Appl. Phys. Lett.*, vol. 96, no. 261109, July 2010.

[26] W. Cao, T. Huang, X. Xu, and H. Elsayed-Ali, "Localized surface plasmon resonance of single silver nanoparticles studies by dark-field optical microscopy and spectroscopy, " *J. Appl. Phys*., vol. 109, no. 034310, pp. 1-6, Feb. 2011.

[27] K. Sendur, "Optical aspects of the interaction of focused beams with plasmonic nanoparticles," *Appl. Comp. Electro. Society (ACES) Journal*, vol. 27, no. 2, pp. 181-188, Feb. 2012.

[28] L. Hammer, M. Schwind, B. Kasemo, and I. Zorić, "Localized surface plasmon resonances in aluminum nanodisks," *Nano Lett.*, vol. 8, no. 5, pp. 1461-1471, Feb. 2008.

[29] M. El-Shenawee, "Polarization dependence of plasmonic nanotoroid dimer antenna," *IEEE Antennas Propagat. Lett.*, vol. 9, pp. 463-466, 2010.

[30] M. El-Shenawee, P. Blake, A. M. Hassan, and D. K. Roper, "Surface plasmons of finite nanoring arrays," *Proc. of the IEEE International Symposium on Antennas and Propagation and USNC/URSI National Radio Science Meeting*, pp. 1609-1612, 2011

[31] N. Large, J. Aizpurua, V. Lin, S. Teo, R. Marty, S. Tripathy, and A. Mlayah, "Plasmonic properties of gold ring-disk nano-resonators: fine shape details matter," *Optics Express*, vol. 19, no. 6, pp. 5587-5595, Mar. 2011.

[32] M. El-Shenawee, D. Macias, A. Baudrion, and R. Bachelot, "Torus nano-antenna: enhanced field and radiation pattern," *Proc. of the IEEE Int. Symp. on Antennas and Prop., and USNC/URSI National Radio Science Meeting*, Charleston SC, USA, June 1-5, 2009.

[33] A. Mary, D. Koller, A. Hohenau, J. Krenn, A. Bouhelier, and A. Dereux, "Optical absorption of torus-shaped metal nanoparticles in the visible range," *Phys. Rev. B*, vol. 76, no. 245422, pp. 1-5, 2007.

[34] K. Nakayama, K. Tanabe, and H. Atwater, "Plasmonic nanoparticle enhanced light absorption in GaAs solar cells," *Appl. Phys. Lett.*, vol. 93, no. 121904, pp. 1-3, Sept. 2008.

[35] Y. Akimov and W. Koh, "Resonant and nonresonant plasmonic nanoparticle enhancement for thin-film silicon solar cells," *Nanotechnology*, vol. 21, no. 235201, pp. 1-6, May 2010.

[36] V. Kochergin, L. Neely, C. Jao, and H. Robinson, "Aluminum plasmonic nanostructures for improved absorption in organic photovoltaic devices," *Appl. Phys. Lett.*, vol. 98, no. 133305, pp. 1-3, Mar. 2011.

[37] N. Burford, M. El-Shenawee, S. Shumate, D. Hutchings, and H. Naseem, "Field enhancement due to surface structuring during aluminum induced crystallization of amorphous silicon," *Proc. of the IEEE Int. Symp. on Antennas and Prop. and USNC/URSI National Radio Science Meeting*, Chicago, USA, July 8-13, 2012.

[38] Z. Wang, L. Jeurgens, J. Wang, and E. Mittemeijer, "Fundamentals of metal-induced crystallization of amorphous semiconductors," *Advanced Eng. Materials*, vol. 11, no. 3, 2009.

[39] S. D. Shumate, M. K. Hafeezuddin, H. A. Naseem, and D. A. Hutchings, "Microstructural influence of hydrogenated amorphous silicon on polycrystalline emitter solar cells prepared by top-down aluminum induced crystallization," P*roc. of the 2011 IEEE PVSC*, Seattle, Washington, June 19-24, 2011.

[40] J. Hoffmann, C. Hafner, P. Leidenberger, J. Hasselbarth, and S. Burger, "Comparison of electromagnetic field solvers for the 3D analysis of plasmonic nano antennas," *Proc. SPIE*, vol. 7390, pp. 73900J-73900J-11, 2009.

[41] A. M. Hassan and M. El-Shenawee, "Mathematical modeling of breast lesion growth" *Proceedings of the Annual Review of Progress in Applied Computational Electromagnetics*, pp. 86-91, Niagara Falls, Canada, March 30 -April 4, 2008.

[42] E. Palik, *Handbook of Optical Constants of Solids*, New York: Academic, 1985.

[43] J. M. Taboada, M. G. Araújo, J. Rivero, L. Landesa, and F. Obelleiro, "Surface integral equation solvers for large-scale conductors, metamaterials and plasmonic nanostructures," *Applied Computational Electromagnetics Society (ACES) Journal*, vol. 27, no. 2, pp. 189-197, Feb. 2012.

**Nathan M. Burford** received his B.Sc. in Physics from Southeast Missouri State University in 2011. He is currently finishing his M.Sc. in Microelectronics-Photonics at the University of Arkansas and will be pursuing a Ph.D. in the same field starting in the summer of 2013. His research interest includes computational design of plasmonic nano-antennas and solar cells, electromagnetic metamaterials and THz imaging and spectroscopy. Mr. Burford is a member of Sigma Pi Sigma honor society and is an NSF GK-12 Fellow.

**Magda El-Shenawee** (M'91–SM'02) received the Ph.D. degree in Electrical Engineering from the University of Nebraska, Lincoln, in 1991. After obtaining her Ph.D., she joined the Center for Electro-Optics as a Research Associate from 1992 to 1994, focusing on the enhanced backscatter phenomenon from random rough ground surfaces. She furthered her research at the National Research Center, Cairo, Egypt, from 1994 to 1996, then at the University of Illinois at Urbana-Champaign, Urbana, from 1997 to 1999. Directly before joining the University of Arkansas faculty, she served as a member of the Multidisciplinary University Research Initiative team working on the antipersonnel landmine detection at Northeastern University, Boston, MA, from 1999 to 2001. Currently, she is a Professor of Electrical Engineering with the University of Arkansas in Fayetteville where she joined as an Assistant Professor in 2001. Her current research interests involve terahertz imaging and spectroscopy, computational inverse scattering algorithms, MEMS antennas, nano-antennas for energy enhancement of photovoltaic solar cells, and biomedical engineering applications to breast cancer using biopotentials and biological tumor growth modeling. Dr. El-Shenawee is a member of Eta Kappa Nu Electrical Engineering honor society.